S1 Interfacial zeta-potential closures

S1.1 General assumptions

The equations in this section define the local zeta potential, ζ, used in the electroosmotic slip condition in Eq. (3) of the main manuscript. Unless otherwise stated, references in this Supplement to equations, reactions, figures, tables, and sections without an "S" prefix refer to the main manuscript. The interfacial state is evaluated using either a one-pK electric-double-layer (EDL) closure or a two-pK extended triple-layer (ETL) closure. Both closures are evaluated under local equilibrium using the aqueous composition immediately adjacent to each grain surface.

The thermodynamic equilibrium relations are formally expressed in terms of aqueous activities. In the numerical implementation, activity coefficients are set to unity, and activities are therefore approximated by molar concentrations. This approximation is applied consistently across all simulations. At C_b = 100 mM, non-ideal activity effects may influence the quantitative magnitude of the predicted interfacial response; the TO–TT–TH sequence is therefore interpreted primarily in terms of concentration-dependent trends within the ETL formulation. The calculated zeta potential determines the local electroosmotic mobility applied in Eq. (3). The interfacial closures do not introduce explicit surface-reaction source or sink terms into the aqueous species balances.

S1.2 One-pK electric-double-layer closure

The one-pK EDL closure represents a single amphoteric surface site, $>\mathrm{MeOH}$, whose charge is regulated by proton exchange. Here, $>\mathrm{Me}$ denotes a generic surface metal centre. The surface reaction is written as (de Lima et al., 2010a; de Lima et al., 2010b; Zhang and Wang, 2017; Yang et al., 2022):

$$(>\mathrm{Me\text{-}OH})^{-1/2} + \mathrm{H}^{+} \leftrightarrow (>\mathrm{Me\text{-}OH_2})^{+1/2}\,. \tag{S1}$$

Under local equilibrium, the surface charge density σ is obtained by combining the mass-action expression for the surface reaction with the diffuse-layer Grahame relation. This yields two equivalent expressions for σ (C·m^{-2}), from which ζ can be solved as a function of local proton concentration and ionic strength (de Lima et al., 2010b):

$$\sigma = \frac{\mathrm{F}\Gamma_{\max}}{2}\left(\frac{KC^{b}_{H^+}\,exp\left(-\frac{\mathrm{F}\zeta}{\mathrm{RT}}\right)-1}{KC^{b}_{H^+}\,exp\left(-\frac{\mathrm{F}\zeta}{\mathrm{RT}}\right)+1}\right) = \sqrt{8\varepsilon_0\varepsilon_r \mathrm{RT}C^{\mathrm{SI}}_b}\,\sinh\left(\frac{\mathrm{F}\zeta}{2\mathrm{RT}}\right), \tag{S2}$$

$$\zeta \approx \begin{cases} -\left[ln\,h + ln\left(1+\frac{1-h}{h}\frac{2A\sqrt{hC^{\mathrm{SI}}_b}}{1+2A\sqrt{hC^{\mathrm{SI}}_b}}\right)\right]\frac{\mathrm{RT}}{\mathrm{F}} \\ \text{with: } h = \left(KC^{b}_{H^+}\right)^{-1} = 10^{pH-pK}; \quad A = \frac{\sqrt{8\varepsilon_0\varepsilon_r \mathrm{RT}}}{\mathrm{F}\Gamma_{\max}} \end{cases}. \tag{S3}$$

Here, $C_{\mathrm{H}^+}^{b}$ and C_b, both expressed in mol·L^{-1} in Eqs. (S2)–(S3), are the aqueous concentrations of hydrogen ions and background electrolyte immediately adjacent to the surface, respectively. The SI concentration used in the Grahame relation is $C_b^{\mathrm{SI}} = 1000\ C_b$, expressed in mol·m^{-3}. R (J·mol^{-1}·K^{-1}) is the universal gas constant; F (C·mol^{-1}) is the Faraday constant; T (K) is the absolute temperature; ε_0 (F·m^{-1}) is the vacuum permittivity; and ε_{r} (-) is the relative permittivity of the aqueous phase. The parameter $\Gamma_{\max}$ (mol·m^{-2}) is the maximum surface-site density. The equilibrium parameter in the one-pK closure is defined here as $pK = \log_{10} K$, consistent with Eq. (S3).

S1.3 Two-pK extended triple-layer closure

The two-pK ETL closure represents two acid–base reactions of amphoteric surface sites together with specific adsorption of the background cation. In the present simulations, $\mathrm{M}^+ = \mathrm{Na}^+$, whereas specific adsorption of Cl^- is not included. The retained surface reactions are (Wang and Revil, 2010):

$$(>\text{Me-OH}_2)^+ \rightleftarrows (>\text{Me-OH}) + \mathrm{H}^+, \quad K_{a1}^{\mathrm{int}}, \tag{S4}$$

$$(>\text{Me-OH}) \rightleftarrows (>\text{Me-O})^- + \mathrm{H}^+, \quad K_{a2}^{\mathrm{int}}, \tag{S5}$$

$$(>\text{Me-O})^- + \mathrm{M}^+ \rightleftarrows (>\text{Me-OM}), \quad K_{M}^{\mathrm{int}}, \tag{S6}$$

where K_{a1}^{int}, K_{a2}^{int}, and $K_{\mathrm{M}}^{\mathrm{int}}$ are the intrinsic equilibrium constants for the first acid dissociation, second acid dissociation, and cation adsorption reactions, respectively. The intrinsic acid-dissociation constants are constrained by the prescribed point of zero charge according to (Papirer, 2000; Leroy et al., 2007):

$$\mathrm{pH(pzc)} = \tfrac{1}{2}\left(pK_{a1}^{\mathrm{int}} + pK_{a2}^{\mathrm{int}}\right), \quad pK_{aj}^{\mathrm{int}} = -\log_{10} K_{aj}^{\mathrm{int}}, \quad j = 1{,}2\,. \tag{S7}$$

Application of the mass-action relations gives the distribution of the surface species as a function of the adjacent aqueous concentrations and the electric potentials at the surface and Stern planes:

$$K_{a1}^{\mathrm{int}} = \frac{\sigma_{(>\text{Me-OH})}}{\sigma_{(>\text{Me-OH}_2)^+}} C_{\mathrm{H}^+}^{b} \exp\left(-\frac{F\psi_0}{RT}\right), \tag{S8}$$

$$K_{a2}^{\mathrm{int}} = \frac{\sigma_{(>\text{Me-O})^-}}{\sigma_{(>\text{Me-OH})}} C_{\mathrm{H}^+}^{b} \exp\left(-\frac{F\psi_0}{RT}\right), \tag{S9}$$

$$K_{\mathrm{M}}^{\mathrm{int}} = \frac{\sigma_{(>\text{Me-OM})}}{\sigma_{(>\text{Me-O})^-}} \frac{1}{C_{\mathrm{M}^+}^{b}} \exp\left(-\frac{F\psi_\beta}{RT}\right). \tag{S10}$$

Here, ψ_0 and ψ_β are the electric potentials at the surface plane and Stern plane, respectively (Fig. 1a). The quantities σ_j denote the charge-equivalent areal densities assigned to the corresponding surface species. They are auxiliary surface-state variables and are not individually equivalent to the net electrical charge of an interfacial plane.

The total abundance of reactive surface sites is constrained by the surface-site balance:

$$\frac{F\Gamma_0}{N_A} = \sigma_{(>\text{Me-OH})} + \sigma_{(>\text{Me-O})^-} + \sigma_{(>\text{Me-OH}_2)^+} + \sigma_{(>\text{Me-OM})} \,, \tag{S11}$$

where Γ_0 is the total surface-site density and N_A is the Avogadro constant. When Γ_0 is reported in sites per unit area, the factor F/N_A converts it to a charge-equivalent areal density consistent with the σ_j variables.

The net charges associated with the surface plane and Stern plane are obtained from the surface-species distributions as:

$$Q_0 = \sigma_{(>\text{Me-OH}_2)^+} - \sigma_{(>\text{Me-O})^-} - \sigma_{(>\text{Me-OM})} \,, \tag{S12}$$

$$Q_\beta = \sigma_{(>\text{Me-OM})} \,. \tag{S13}$$

The diffuse-layer charge density is related to the diffuse-layer potential through the Gouy–Chapman relation:

$$Q_d = -\sqrt{\frac{8\varepsilon_0\varepsilon_r RTN_s^b}{N_A}}\sinh\left(\frac{F\psi_d}{2RT}\right), \text{ with: } N_s^b = 1000N_A\left(C_{M^+}^b + C_{H^+}^b\right) . \tag{S14}$$

Here, Q_0, Q_β, and Q_d are the net charge densities associated with the surface, Stern, and diffuse-layer planes, respectively; ψ_d is the diffuse-layer potential; and N_s^b is the bulk number concentration of mobile cations used in the Gouy–Chapman relation. The factor of 1000 converts concentrations expressed in mol·L^{-1} to mol·m^{-3}.

Electroneutrality across the interfacial region and the two Stern-layer capacitance relations close the ETL system:

$$Q_0 + Q_\beta + Q_d = 0 \,, \tag{S15}$$

$$\psi_0 - \psi_\beta = Q_0/C_1 \,, \tag{S16}$$

$$\psi_\beta - \psi_d = -Q_d/C_2 \,, \tag{S17}$$

where C_1 and C_2 are the integral capacitances of the inner and outer Stern-layer regions, respectively. The diffuse-layer potential, ψ_d, is identified with the shear-plane zeta potential, ζ.

S1.4 Numerical solution

The coupled nonlinear equations for ψ_0, ψ_β, ψ_d, and the associated surface-state variables were solved in COMSOL using a damped Newton method at each time step. The converged solution from the preceding time step was used as the initial estimate for the subsequent step. A relative nonlinear-solver tolerance of 5×10^{-3} was used in the production simulations. Representative ETL cases were repeated using relative tolerances of 10^{-3} and 10^{-4}. Changes in ζ, electroosmotic mobility, and the reported plume descriptors were negligible relative to the contrasts among cases, indicating that the representative responses were insensitive to nonlinear-solver tolerance over the tested range.

S2 Electrolysis-driven electrode boundary conditions

S2.1 Ionic current and electrolysis source fluxes

For the water-electrolysis reactions given in Reactions (R1) and (R2), the ionic current density was calculated from the Nernst–Planck fluxes of all charged aqueous species:

$$\boldsymbol{i} = \mathrm{F}\sum_{i=1}^{N_{\mathrm{ion}}} z_i \boldsymbol{J}_i \,, \tag{S18}$$

where $\boldsymbol{i}$ (A·m^{-2}) is the ionic current-density vector, N_{ion} is the number of charged aqueous species, and $\boldsymbol{J}_i$(mol·m^{-2}·s^{-1}) is the Nernst–Planck flux of species i, as defined in Eq. (4). Electrical conduction through the solid grains is not included.

At electrode boundary e, the outward normal ionic current density is

$$j_e = \boldsymbol{i}\cdot\boldsymbol{n_e}, \quad e \in \{A, C\}\,, \tag{S19}$$

where $\boldsymbol{n}_e$ is the unit normal directed outward from the pore domain towards the corresponding electrode chamber. Under the fixed electrode polarity used here, the stoichiometry of Reactions (R1) and (R2) gives one mole of $\mathrm{H^+}$ or $\mathrm{OH^-}$ per mole of transferred electrons. The corresponding electrolysis-production fluxes are therefore

$$J^{\mathrm{we}}_{\mathrm{H^+},A} = \frac{|j_A|}{F}, \quad J^{\mathrm{we}}_{\mathrm{OH^-},C} = \frac{|j_C|}{F}\,. \tag{S20}$$

The electrolysis-production flux is zero for $\mathrm{H^+}$ at the cathode, for $\mathrm{OH^-}$ at the anode, and for $\mathrm{Na^+}$, $\mathrm{Cl^-}$, and Org at both electrodes.

S2.2 Electrode-chamber mass balance

Each lateral electrode boundary was coupled to an idealized well-mixed electrode chamber. For species i at electrode e, the chamber concentration was updated according to:

$$\frac{\partial C_{i,e}}{\partial t} = \alpha_e\left(J_{i,e} + J^{we}_{i,e}\right)\,, \tag{S21}$$

$$J_{i,e} = \boldsymbol{J}_i\cdot\boldsymbol{n}_e, \quad \alpha_e = \frac{A_e}{V_e}\,, \tag{S22}$$

where $C_{i,e}$ (mol·m^{-3}) is the well-mixed concentration in electrode chamber e, $J_{i,e}$ is the species flux leaving the pore domain and entering the chamber, and $J^{\mathrm{we}}_{i,e}$ is the electrolysis-production flux. The quantities A_e and V_e are the effective electrode–pore interface area and chamber volume, respectively, and α_e therefore has units of m^{-1}. The same area-to-volume ratio, $\alpha_A = \alpha_C$ =10^{-4} m^{-1}, was applied to both electrode chambers in this study. With the outward-normal convention in Eq. (S22), positive $J_{i,e}$ increases the corresponding chamber concentration.

The calculated chamber concentrations were imposed as spatially uniform, time-dependent concentration conditions at the corresponding lateral boundaries. They were updated together with the evolving ionic fluxes at each time step. Electrode pH

therefore evolved from the coupled transport solution and electrolysis source terms rather than being imposed as a prescribed time series.

S2.3 Water autoionization and pH calculation

Water autoionization was assumed to remain at instantaneous equilibrium:

$$a_{H^+} a_{OH^-} = K_w \ . \tag{S23}$$

Activity coefficients were set to unity. When concentrations are expressed in mol·L^{-1}, the concentration product at 298.15 K is:

$$C_{H^+} C_{OH^-} = 10^{-14} (\mathrm{mol} \cdot \mathrm{L}^{-1})^2 \ . \tag{S24}$$

The corresponding pH was calculated from:

$$\mathrm{pH} = -\log_{10} C_{H^+} \ . \tag{S25}$$

S2.4 Species-specific boundary conditions

The initial and electrode-boundary conditions are summarized in Table S2. At the anode, $C_{H^+,A}$ was updated from the chamber mass balance including the electrolysis source, whereas $C_{OH^-,A}$ was obtained from water autoionization. At the cathode, $C_{OH^-,C}$ was updated from the chamber mass balance including the electrolysis source, whereas $C_{H^+,C}$ was obtained from water autoionization. The background-ion concentrations were updated from their normal Nernst–Planck fluxes without electrode-reaction source terms. Org was not included in the electrode-chamber mass balances; both lateral boundaries were assigned $C_{Org} = 0$, consistent with the symmetric sink conditions described in Sect. 2.3.2.

S3 Stage-aligned plume analysis

S3.1 Selection of stage-aligned observation times

The normalized within-window progress variable, $P(t)$, is defined in Eq. (14). By definition, $P(0) = 0$ and $P(t_{\mathrm{end}}) = 1$, where t_{end} = 30 min. The target level $p_s = 1$ therefore represents the first attainment of the CMZ depletion observed at t_{end}. It may occur before t_{end} if the CMZ concentration subsequently exhibits a small rebound and does not imply complete Org depletion. Small non-monotonic variations in the discrete $P(t)$ series may result from transient tracer redistribution or numerical fluctuations. To obtain a unique first-attainment time for each target level, the series was transformed using a cumulative maximum:

$$P_{mono}(t_i) = \max_{0 \le j \le i} P(t_j) \, . \tag{S26}$$

For a target progress level p_s, the smallest output index $i$satisfying $P_{\mathrm{mono}}(t_i) \ge p_s$ was identified. The corresponding stage time was calculated by linear interpolation:

$$t_{p_s} = t_{i-1} + \frac{p_s - P_{mono}(t_{i-1})}{P_{mono}(t_i) - P_{mono}(t_{i-1})} (t_i - t_{i-1}) \, . \tag{S27}$$

Stage-aligned fields were evaluated at p_s = 0.25, 0.60, and 1.00. Because the stored model-output interval was Δt_{out} = 0.05 min, the concentration field used for spatial analysis was extracted from the stored output nearest to the interpolated t_{p_s}, whereas the interpolated value was retained when reporting the stage-attainment time. The cumulative-maximum transformation was used only to identify the stage time; all spatial descriptors were calculated from the original simulated concentration fields.

S3.2 Spatial moments and plume orientation

At each stage time t_{p_s}, plume position and shape were calculated from the two-dimensional Org concentration field, $C_{\mathrm{Org}}(\boldsymbol{x}, t_{p_s})$, over the fluid-filled analysis domain Ω_a of the computational domain. For each case, the analysis domain covered the full fluid-filled computational domain and remained fixed across all progress stages. The external vertical extent was geometry-specific, as described in Sect. 2.2.1 of the main manuscript. The zeroth spatial moment is

$$M_0(t_{p_s}) = \int_{\Omega_a} C_{\mathrm{Org}}(\boldsymbol{x}, t_{p_s}) d\Omega \, . \tag{S28}$$

In the two-dimensional model, M_0 is proportional to the dissolved Org mass per unit out-of-plane thickness. The plume centroid is defined as

$$\widetilde{v_i}(t_{p_s}) = \frac{1}{M_0(t_{p_s})} \int_{\Omega_a} x_i C_{Org}(\boldsymbol{x}, t_{p_s}) d\Omega \, , \quad i \in \{x, y\} \, . \tag{S29}$$

The concentration-weighted covariance tensor is

$$\mathbf{COV} = \begin{bmatrix} COV_{xx} & COV_{xy} \\ COV_{yx} & COV_{yy} \end{bmatrix}, \tag{S30}$$

with

$$COV_{ij} = \frac{1}{M_0(t_{p_s})} \int_{\Omega_a} (x_i - \tilde{v}_i)(x_j - \tilde{v}_j) C_{\mathrm{Org}}(\boldsymbol{x}, t_{p_s}) d\Omega, \quad i,j \in \{x,y\} . \tag{S31}$$

The principal-axis orientation, measured counterclockwise from the x-axis, is calculated as

$$\theta = \frac{1}{2}\mathrm{atan2}\left(2COV_{xy}, COV_{xx} - COV_{yy}\right) . \tag{S32}$$

The resulting angle was converted from radians to degrees for presentation. Because a principal axis has no intrinsic direction, orientations differing by 180° are equivalent. With the adopted implementation, θ lies within [−90°, 90°].

The eigenvalues of $\mathbf{COV}$ are:

$$\lambda_{1,2} = \frac{1}{2}\left[\left(COV_{xx} + COV_{yy}\right) \pm \sqrt{\left(COV_{xx} - COV_{yy}\right)^2 + 4COV_{xy}^2}\right], \quad (\lambda_1 \geq \lambda_2 \geq 0) . \tag{S33}$$

The plume-anisotropy ratio is

$$R_P = \frac{\lambda_1}{\lambda_2} . \tag{S34}$$

The eigenvalues have dimensions of squared length. Their square roots represent characteristic plume extents along the major and minor principal axes, whereas R_P is a dimensionless measure of plume elongation. A value of R_P = 1 represents an isotropic second-moment distribution, and larger values indicate stronger elongation.

S3.3 Plume-aligned sampling window

A plume-aligned coordinate system (s, n) was constructed at each stage, with s aligned with the major plume axis and n oriented perpendicular to it. Here, n is a scalar plume-transverse coordinate and is distinct from the grain-surface unit-normal vector $\boldsymbol{n}$ used in Eq. (3). The adaptive rectangular sampling window was centred at $(\tilde{v}_x, \tilde{v}_y)$, with half-lengths:

$$L_s = k_s\sqrt{\lambda_1(t_{p_s})}, \quad L_n = k_n\sqrt{\lambda_2(t_{p_s})} . \tag{S35}$$

The calculations used $k_s = k_n = 6$. The window was discretized using N_s = 500 points along $s \in [-L_s, L_s]$ and N_n = 41 points along $n \in [-L_n, L_n]$. These parameters were applied consistently to all Scenario II cases and stages.

S3.4 Coordinate transformation and field resampling

The forward transform from laboratory coordinates (x, y) to plume-aligned coordinates (s, n) is:

$$\begin{bmatrix} s \\ n \end{bmatrix} = \mathbf{R}^{\mathrm{T}}(\theta)\left(\begin{bmatrix} x \\ y \end{bmatrix} - \begin{bmatrix} \tilde{v}_x \\ \tilde{v}_y \end{bmatrix}\right), \tag{S36}$$

where $\mathbf{R}(\theta)$ is the rotation matrix:

$$\boldsymbol{R}(\theta) = \begin{bmatrix} cos\,\theta & -sin\,\theta \\ sin\,\theta & cos\,\theta \end{bmatrix}. \tag{S37}$$

The inverse transform is

$$\begin{bmatrix} x \\ y \end{bmatrix} = \begin{bmatrix} \tilde{v}_x \\ \tilde{v}_y \end{bmatrix} + \mathbf{R}(\theta)\begin{bmatrix} s \\ n \end{bmatrix}. \tag{S38}$$

For each node (s_i, n_j) of the regular plume-aligned grid, Eq. (S38) was used to determine the corresponding point in the original (x, y) coordinate system. The simulated Org concentration field was then interpolated onto the regular grid to obtain $C_{\mathrm{Org}}^{(sn)}(\mathrm{s}_i, n_j, t_{p_s})$. Grid nodes mapped outside the fluid-filled computational domain were excluded from the transverse projection. The same interpolation procedure was applied to all cases and stages.

S3.5 One-dimensional plume profile

The resampled two-dimensional field was reduced to a one-dimensional profile along the plume principal axis using the maximum concentration across the valid transverse grid nodes:

$$C_{\mathrm{Org}}^{(s)}(s_i, t_{p_s}) = \max_{n_j} C_{\mathrm{Org}}^{(sn)}(s_i, n_j, t_{p_s}), \quad i = 1, \cdots, N_s\,. \tag{S39}$$

The maximum projection was selected to retain locally resolved concentration ridges that could be obscured by transverse averaging. The resulting profile was normalized by its maximum value:

$$\tilde{C}_{\mathrm{Org}}^{(s)}(s_i, t_{p_s}) = \frac{C_{\mathrm{Org}}^{(s)}(s_i, t_{p_s})}{\max_i C_{\mathrm{Org}}^{(s)}(s_i, t_{p_s})}\,. \tag{S40}$$

The normalized profile was smoothed using a seven-point moving-average filter. The same filter width was applied to all cases and stages. Smoothing was used only for peak detection; the original simulated concentration fields were retained for the spatial-moment analysis in Sect. S3.2.

S3.6 Peak detection and spacing metrics

Local maxima in the smoothed profile $\tilde{C}_{\mathrm{Org}}^{(s)}$ were interpreted as resolved concentration ridges along the plume principal axis. These ridges do not correspond directly to individual geometric pores or pore-throat spacings.

Three fixed criteria were used for peak detection. First, the minimum normalized peak height was set to $h_{\min} = 0.05$. Second, the profile amplitude was calculated as $A_P = \max_i \tilde{C}_{\mathrm{Org}}^{(s)}(s_i) - \min_i \tilde{C}_{\mathrm{Org}}^{(s)}(s_i)$ and the minimum peak prominence was defined as:

$$\Pi_{\min} = \min(0.03, 0.5A_P) \,. \tag{S41}$$

Third, the minimum permitted separation between detected peaks was

$$d_{\min} = \max[0.02(s_{\max} - s_{\min}),\ 2\delta s] \,, \tag{S42}$$

where the regular along-axis grid spacing is $\delta s = \frac{s_{\max} - s_{\min}}{N_s - 1} = \frac{2L_s}{N_s - 1}$.

Let the detected peak positions, sorted in increasing s, be $\left\{s_j^{(P)}\right\}_{j=1}^{N_{\mathrm{peaks}}}$. When $N_{\mathrm{peaks}} \geq 2$, the adjacent-peak separations are:

$$\Delta s_j(t_{p_s}) = s_{j+1}^{(P)}(t_{p_s}) - s_j^{(P)}(t_{p_s}), \quad j = 1, \cdots, N_{peaks} - 1 \,. \tag{S43}$$

The characteristic ridge spacing is defined as

$$PS(t_{p_s}) = \mathrm{median}(\{\Delta s_j(t_{p_s})\}) \,, \tag{S44}$$

and the variability of the adjacent-ridge spacing is quantified by

$$PS_{IQR}(t_{p_s}) = \mathrm{IQR}(\{\Delta s_j(t_{p_s})\}) \,. \tag{S45}$$

When $N_{\mathrm{peaks}} < 2$, PS and PS_{IQR} are undefined and are represented by an em dash.

S4 Supplementary tables and figures

This section compiles supplementary model parameters, boundary-condition specifications, case-specific transport metrics, relative-progress timing results, concentration-ridge diagnostics, and additional zone- and electrode-boundary-averaged time series. Tables S1 and S2 summarize the parameters and boundary conditions used in the interfacial-charge and electrode models, respectively. Tables S3–S6 report the case-specific simulation results and plume-analysis metrics, while Figs. S1–S3 provide additional temporal responses supporting the results presented in Sect. 3 of the main manuscript.

Table S1. Parameters used in the one-pK EDL and two-pK ETL interfacial-charge closures.

Closure	Parameter	Symbol	Value	Unit	Source
EDL and ETL	Maximum surface density	Γ_{max}, Γ_0	5	sites·nm^{-2}	
EDL and ETL	Point of zero charge	pH(pzc)	3.5	–	
EDL	One-pK equilibrium parameter	pK	3.5	–	
ETL	First intrinsic acid-dissociation constant	K_{a1}^{int}	$10^{-0.27}$	–	Wang and Revil (2010); Zhang and Zhang (1992); Bray et al. (2014); Liu et al. (2013)
	Second intrinsic acid-dissociation constant	K_{a2}^{int}	$10^{-6.73}$	–	
	Cation-adsorption constant	$K_{\mathrm{M}}^{\mathrm{int}}$	$10^{-0.25}$	–	
	Inner Stern-layer capacitance	C_1	1.07	F·m^{-2}	
	Outer Stern-layer capacitance	C_2	0.2	F·m^{-2}	

Table S2. Initial and time-dependent electrode-boundary conditions for the aqueous species.

Species	Anode boundary	Cathode boundary	Initial value
$\mathrm{H^+}$	$\frac{\partial C_{\mathrm{H^+,A}}}{\partial t} = \alpha_A\left(J_{\mathrm{H^+,A}} + J_{\mathrm{H^+,A}}^{\mathrm{we}}\right)$	$C_{\mathrm{H^+,C}} = K_w / C_{\mathrm{OH^-,C}}$	1.0×10^{-4} mol·m^{-3}
$\mathrm{OH^-}$	$C_{\mathrm{OH^-,A}} = K_w / C_{\mathrm{H^+,A}}$	$\frac{\partial C_{\mathrm{OH^-,C}}}{\partial t} = \alpha_C\left(J_{\mathrm{OH^-,C}} + J_{\mathrm{OH^-,C}}^{\mathrm{we}}\right)$	1.0×10^{-4} mol·m^{-3}
$\mathrm{Na^+}$	$\frac{\partial C_{\mathrm{Na^+,A}}}{\partial t} = \alpha_A J_{\mathrm{Na^+,A}}$	$\frac{\partial C_{\mathrm{Na^+,C}}}{\partial t} = \alpha_C J_{\mathrm{Na^+,C}}$	C_b
$\mathrm{Cl^-}$	$\frac{\partial C_{\mathrm{Cl^-,A}}}{\partial t} = \alpha_A J_{\mathrm{Cl^-,A}}$	$\frac{\partial C_{\mathrm{Cl^-,C}}}{\partial t} = \alpha_C J_{\mathrm{Cl^-,C}}$	C_b
Org	$C_{\mathrm{Org}} = 0$	$C_{\mathrm{Org}} = 0$	CMZ: 1 mol·m^{-3}; Buffer zones: 0

Note: *$J_{i,e} = \boldsymbol{J}_i \cdot \boldsymbol{n}_e$ denotes the outward normal Nernst–Planck flux of species i at electrode e, where $\boldsymbol{n}_e$ points from the pore domain into the corresponding electrode chamber. Thus, $J_{i,e} > 0$ represents transfer from the pore domain into the chamber at both the anode and cathode. $J_{i,e}^{we}$ is a positive electrolysis-production flux and is non-zero only for $\mathrm{H^+}$ at the anode and $\mathrm{OH^-}$ at the cathode.*

Table S3. Case-specific CMZ depletion and late-time persistence metrics for Org.

Scenario	Case	$\eta_{30,CMZ}$	$t_{90,CMZ}$ (min)	TI_{CMZ}
SI	TO0	0.941	10.19	0.060
	TO15	0.960	7.49	0.040
	TO30	0.973	6.68	0.027
	TO45	0.969	7.19	0.031
SII	TOHD	0.956	8.05	0.044
	TOND	0.978	9.71	0.022
SI	TT0	0.888	> 30.00	0.134
	TT15	0.915	17.21	0.091
	TT30	0.930	13.89	0.073
	TT45	0.927	15.78	0.080
SII	TTHD	0.911	18.31	0.096
	TTND	0.937	19.16	0.090
SI	TH0	0.556	> 30.00	0.515
	TH15	0.632	> 30.00	0.442
	TH30	0.642	> 30.00	0.431
	TH45	0.553	> 30.00	0.507
SII	THHD	0.710	> 30.00	0.387
	THND	0.585	> 30.00	0.508
SI	DT0	0.996	3.36	0.004
	DT15	0.998	2.64	0.002
	DT30	0.999	2.44	0.001
	DT45	0.999	2.62	0.001
SII	DTHD	0.998	2.85	0.002
	DTND	0.999	3.59	0.001

Note: *A value of > 30.00 min indicates that 90 % CMZ depletion was not reached within the 30 min simulation window and that $t_{90,CMZ}$ is right-censored. The definitions of $\eta_{30,CMZ}$, $t_{90,CMZ}$, and TI_{CMZ} are given in Eqs. (11)–(13). The depletion fraction and tailing index are dimensionless. Case codes are defined in Table 1.*

Table S4. First-attainment times, t_{p_s}(min), at the selected relative-progress levels for Scenario I.

Case	$t_{0.25}$ (min)	$t_{0.60}$ (min)	$t_{1.00}$ (min)
TO0	1.85	5.00	28.30
TO15	1.55	4.10	22.45
TO30	1.55	3.90	18.90
TO45	1.65	4.20	30.00
TT0	2.65	8.25	30.00
TT15	2.30	6.80	30.00
TT30	2.35	6.50	30.00
TT45	2.50	7.00	30.00
TH0	1.65	11.15	30.00
TH15	2.10	10.85	30.00
TH30	2.35	10.80	30.00
TH45	1.85	9.90	30.00
DT0	0.85	2.05	10.45
DT15	0.70	1.65	8.40
DT30	0.65	1.55	7.30
DT45	0.70	1.70	15.55

Note: *Relative progress is normalized by each case's CMZ depletion at t = 30 min. The quantities $t_{0.25}$, $t_{0.60}$, and $t_{1.00}$ denote the first attainment of 25 %, 60 %, and 100 % of the case-specific within-window depletion, respectively. A value of 30.00 min indicates that the endpoint-equivalent depletion level was first attained at the final saved time; it is neither a right-censored value nor an indication of complete CMZ depletion.*

Table S5. First-attainment times, t_{p_s}(min), at the selected relative-progress levels for the Scenario II composite geometries.

Case	$t_{0.25}$ (min)	$t_{0.60}$ (min)	$t_{1.00}$ (min)
TOHD	1.70	4.40	19.35
TOND	2.30	5.70	29.85
TTHD	2.55	7.25	30.00
TTND	3.65	9.45	30.00
THHD	3.05	12.75	30.00
THND	3.70	13.35	30.00
DTHD	0.75	1.80	5.45
DTND	0.95	2.25	7.20

Note: *Relative progress is normalized by each case's CMZ depletion at t = 30 min. The quantities $t_{0.25}$, $t_{0.60}$, and $t_{1.00}$ denote the first attainment of 25 %, 60 %, and 100 % of the case-specific within-window depletion, respectively. A value of 30.00 min indicates that the endpoint-equivalent depletion level was first attained at the final saved time; it is neither a right-censored value nor an indication of complete CMZ depletion.*

Table S6. Plume-aligned concentration-ridge detection and spacing metrics for the Scenario II composite geometries.

Case	p_s	N_{peaks}	PS(m)	PS_{IQR}(m)
TOHD	0.25	1	—	—
	0.60	1	—	—
	1.00	0	—	—
TTHD	0.25	1	—	—
	0.60	1	—	—
	1.00	0	—	—
THHD	0.25	1	—	—
	0.60	1	—	—
	1.00	0	—	—
DTHD	0.25	2	1.3×10^{-3}	0
	0.60	1	—	—
	1.00	1	—	—
TOND	0.25	1	—	—
	0.60	1	—	—
	1.00	0	—	—
TTND	0.25	1	—	—
	0.60	1	—	—
	1.00	0	—	—
THND	0.25	1	—	—
	0.60	1	—	—
	1.00	0	—	—
DTND	0.25	1	—	—
	0.60	5	1.8×10^{-4}	3.5×10^{-4}
	1.00	0	—	—

Note: *PS and PS_{IQR} are defined only when $N_{peaks} \geq 2$. An em dash indicates that fewer than two peaks were detected and that the spacing metrics are therefore undefined. When $N_{peaks} = 2$, $PS_{IQR} = 0$ because only one adjacent-peak separation is available; this value is not an estimate of statistical uncertainty.*

Figure S1. Zone- and electrode-boundary-averaged time series for Scenario I.

Panels (a–c) show the temporal evolution of zone-averaged porewater speed, $\langle U \rangle_{\Omega_k}$, in the anode buffer zone (ABZ), contaminated medium zone (CMZ), and cathode buffer zone (CBZ), respectively. Panels (d–f) show the anode-boundary-averaged Na^+ concentration, Cl^- concentration, and pH, and panels (g–i) show the corresponding cathode-boundary averages. Colours denote the TO, TT, TH, and DT electrochemical groups. Solid curves show means across the four SROE orientations within each group, and shaded bands indicate ±1 standard deviation among those deterministic geometries. Logarithmic axes are identified in the corresponding panels.

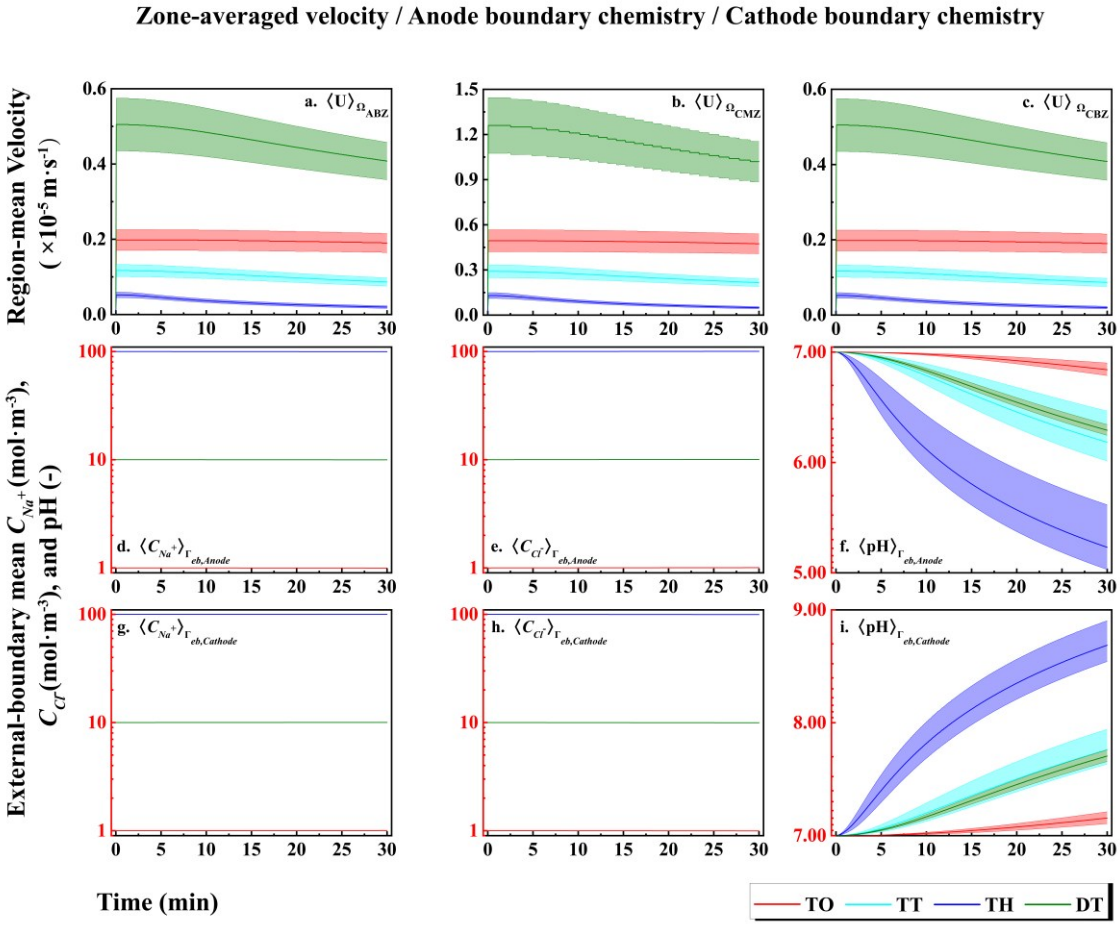

Figure S2. Temporal evolution of zone-averaged Org concentration and pH for the Scenario II composite geometries.

Panels (a–c) show Org concentration in the anode buffer zone (ABZ), contaminated medium zone (CMZ), and cathode buffer zone (CBZ), respectively, and panels (d–f) show the corresponding zone-averaged pH. Colours denote the TO, TT, TH, and DT electrochemical groups. Solid curves show arithmetic means across the HD and ND geometries within each group, and shaded envelopes span the two geometry-specific values.

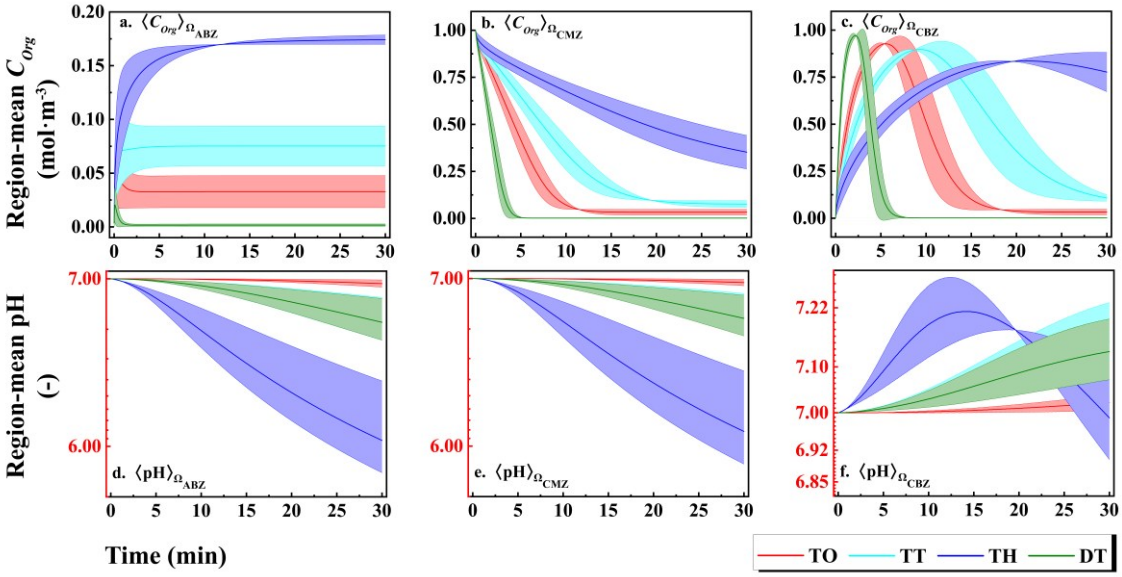

Figure S3. Zone- and electrode-boundary-averaged time series for Scenario II.

Panels (a–c) show the temporal evolution of zone-averaged porewater speed, $\langle U \rangle_{\Omega_k}$, in the anode buffer zone (ABZ), contaminated medium zone (CMZ), and cathode buffer zone (CBZ), respectively. Panels (d–f) show the anode-boundary-averaged Na^+ concentration, Cl^- concentration, and pH, and panels (g–i) show the corresponding cathode-boundary averages. Colours denote the TO, TT, TH, and DT electrochemical groups. Solid curves show arithmetic means across the HD and ND geometries within each group, and shaded envelopes span the two geometry-specific values. Logarithmic axes are identified in the corresponding panels.

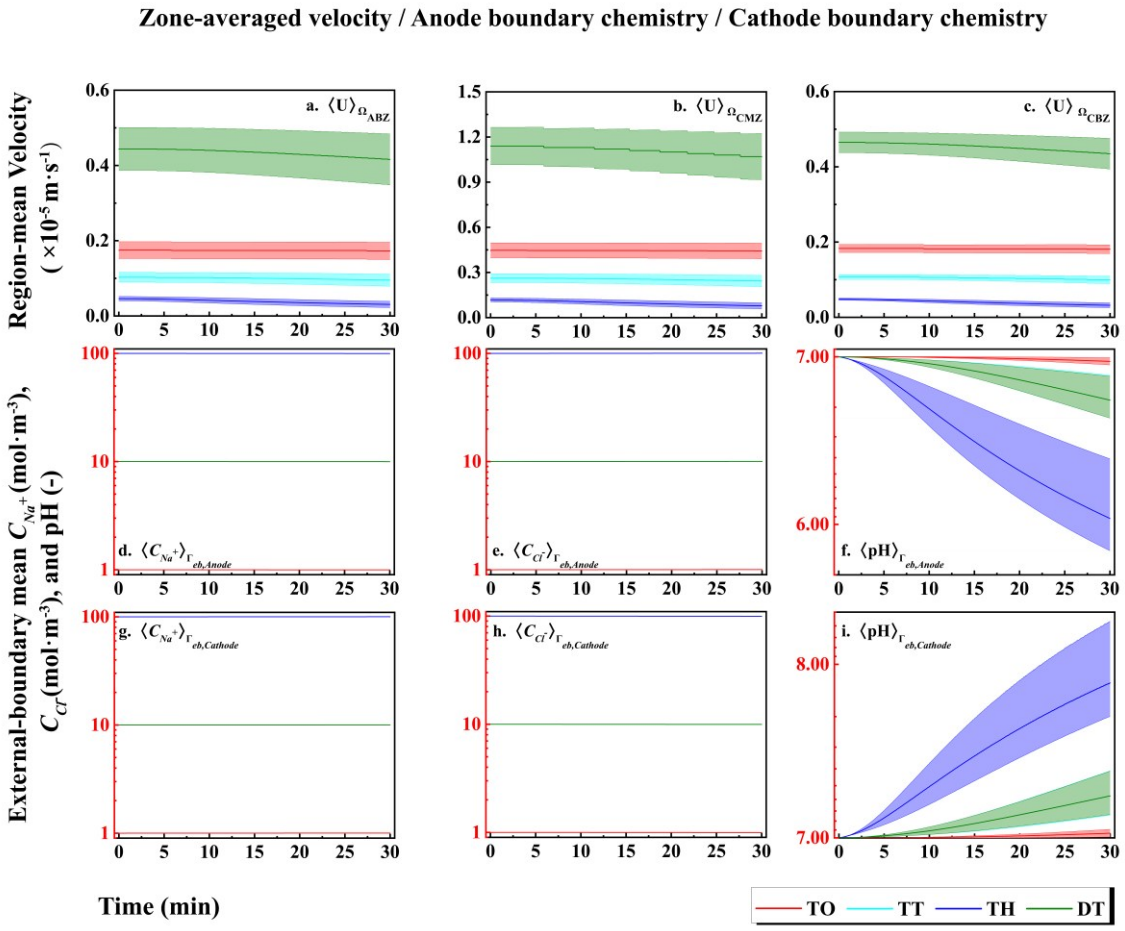

S5 Numerical convergence assessment

Spatial- and temporal-discretization sensitivity was assessed using the representative TT30 case. The mesh analysis compared M1, M2, and M3, containing 43,986, 84,134, and 165,478 elements, respectively. M2 was the production mesh used for the simulations reported in the main manuscript, whereas M3 was used only as the fine-reference solution. Maximum-time-step sensitivity was evaluated on M2 using the production maximum internal time step, $\Delta t_{\max}$, and reduced settings of $\Delta t_{\max}/2$ and $\Delta t_{\max}/4$. The initial BDF step, 30 min simulation window, and 0.05 min saved-output interval were unchanged.

Across the five principal transport metrics, differences between M2 and M3 were at most 0.421%, whereas differences between the production and quarter-maximum-step simulations were at most 1.445% (Table S7a–b). The relative L2 differences in the time-dependent f_{CMZ} profile were 0.065% and 0.283% for the mesh and maximum-time-step assessments, respectively. The corresponding differences in the porewater-flow and electrokinetic profiles were at most 0.0041% and 0.0002% (Table S7c). The close agreement indicates that M2 and the production maximum-time-step setting provide sufficiently converged results for the comparisons reported in this study. The supporting summary data and figures are archived in the associated Figshare repository (Wu et al., 2026).

Table S7. Sensitivity of TT30 transport metrics and time-dependent profiles to mesh refinement and maximum-time-step reduction. M2 and the production maximum-time-step setting were used for the simulations reported in the main manuscript.

(a) Mesh sensitivity

Metric	Unit	M1 coarse	M2 production	M3 fine reference	M1–M2 difference (%)	M2–M3 difference (%)
$\eta_{30,\mathrm{CMZ}}$	–	0.929888	0.929902	0.929902	0.002	0.000
$t_{90,\mathrm{CMZ}}$	min	13.919	13.885	13.944	0.244	0.421
TI_{CMZ}	–	0.0733922	0.0733652	0.0734467	0.037	0.111
$t_{0.25}$	min	2.344	2.343	2.342	0.049	0.033
$t_{0.60}$	min	6.481	6.478	6.479	0.051	0.019

(b) Maximum-time-step sensitivity on M2

Metric	Unit	Production $\Delta t_{\max}$	$\Delta t_{\max}/2$	$\Delta t_{\max}/4$, reference	Production–quarter difference (%)	Half–quarter difference (%)
$\eta_{30,\mathrm{CMZ}}$	–	0.929902	0.929831	0.929810	0.010	0.002
$t_{90,\mathrm{CMZ}}$	min	13.885	13.981	14.089	1.445	0.764
TI_{CMZ}	–	0.0733652	0.0737690	0.0740385	0.909	0.364
$t_{0.25}$	min	2.343	2.342	2.342	0.012	0.003
$t_{0.60}$	min	6.478	6.477	6.472	0.090	0.081

(c) Time-dependent profile differences

Profile	M2–M3 relative L2 difference (%)	Production–quarter relative L2 difference (%)
f_{CMZ}	0.06518	0.28317
$\langle U \rangle_{\Omega_{\mathrm{CMZ}}}$	0.00364	0.00019
$\langle \zeta \rangle_{\Gamma_{\mathrm{ib,CMZ}}}$	0.00059	0.00019
$\langle \mu_{\mathrm{eo}} \rangle_{\Gamma_{\mathrm{ib,CMZ}}}$	0.00059	0.00019
$\langle E_{t,x} \rangle_{\Gamma_{\mathrm{ib,CMZ}}}$	0.00191	4.10×10^{-7}
$\langle u_{\mathrm{eo},x} \rangle_{\Gamma_{\mathrm{ib,CMZ}}}$	0.00240	0.00019

Profile	M2–M3 relative L2 difference (%)	Production–quarter relative L2 difference (%)
$\langle E_{t,y} \rangle_{\Gamma_{\mathrm{ib,CMZ}}}$	0.00358	4.22×10^{-7}
$\langle u_{\mathrm{eo},y} \rangle_{\Gamma_{\mathrm{ib,CMZ}}}$	0.00406	0.00019

Note: *Scalar relative differences were calculated as* $\delta = 100 \mid Q - Q_{ref} \mid / \mid Q_{ref} \mid$. *M2 was the reference for the M1–M2 comparison, M3 for the M2–M3 comparison, and the quarter-maximum-step simulation for the temporal comparisons. Profile differences were calculated as* $\delta_{L2} = 100 \parallel Q - Q_{ref} \parallel_2 / \parallel Q_{ref} \parallel_2$ *over 0–30 min. Percentages were calculated from the unrounded values.*

References

Bray, A. W., Benning, L. G., Bonneville, S., and Oelkers, E. H.: Biotite surface chemistry as a function of aqueous fluid composition, Geochimica Et Cosmochimica Acta, 128, 58-70, 10.1016/j.gca.2013.12.002, 2014.

de Lima, S. A., Murad, M. A., Moyne, C., and Stemmelen, D.: A three-scale model of pH-dependent flows and ion transport with equilibrium adsorption in kaolinite clays: I. Homogenization analysis, Transp. Porous Media, 85, 23-44, 10.1007/s11242-010-9545-4, 2010a.

de Lima, S. A., Murad, M. A., Moyne, C., Stemmelen, D., and Boutin, C.: A three-scale model of pH-dependent flows and ion transport with equilibrium adsorption in kaolinite clays: II Effective-medium behavior, Transp. Porous Media, 85, 45-78, 10.1007/s11242-010-9546-3, 2010b.

Leroy, P., Revil, A., Altmann, S., and Tournassat, C.: Modeling the composition of the pore water in a clay-rock geological formation (Callovo-Oxfordian, France), Geochimica Et Cosmochimica Acta, 71, 1087-1097, 10.1016/j.gca.2006.11.009, 2007.

Liu, Y. J., Naidu, R., and Ming, H.: Surface electrochemical properties of red mud (bauxite residue): Zeta potential and surface charge density, J. Colloid Interface Sci., 394, 451-457, 10.1016/j.jcis.2012.11.052, 2013.

Papirer, E.: Adsorption on Silica Surfaces, Adsorption on Silica Surfaces, New York2000.

Wang, M. and Revil, A.: Electrochemical charge of silica surfaces at high ionic strength in narrow channels, J. Colloid Interface Sci., 343, 381-386, 10.1016/j.jcis.2009.11.039, 2010.

Wu, W., Pan, G., Dai, H., Yang, J., and Yang, P.: Source data, pore-scale structure files, geometry-generation outputs, and numerical-convergence results for "Transient electroosmotic transport under evolving pH and contrasting background electrolyte concentrations: coupled controls of interfacial charge and pore structure", *Figshare [data set and code]*, https://figshare.com/s/c705e08395c02dc48375, 2026.

Yang, P., Ye, S. J., Wu, J. F., and Wu, J. C.: Process-based pore-scale simulation of electrokinetic remediation of organic pollutant in porous media, J. Hydrol., 613, 15, 10.1016/j.jhydrol.2022.128436, 2022.

Zhang, H. and Zhang, X. N.: Electrokinetic properties of ferralsols in china in relation to pedogenic development, Geoderma, 54, 173-188, 1992.

Zhang, L. and Wang, M. R.: Electro-osmosis in inhomogeneously charged microporous media by pore-scale modeling, J. Colloid Interface Sci., 486, 219-231, 10.1016/j.jcis.2016.09.057, 2017.